Journal Pre-proof

Methane seepage dynamics and ground heating phenomena in the southern Po Valley: the case study of Santa Maria Nuova (Italy)

Capelli Ghioldi G., Tamburello G., Sciarra A., Rouwet D., Ricci T., Civico R., Tassi F., Severi P., Liuzzo M., Coltorti M., Rizzo A.L.

PII: S0883-2927(25)00288-4

DOI: https://doi.org/10.1016/j.apgeochem.2025.106565

Reference: AG 106565

To appear in: *Applied Geochemistry*

Received Date: 24 February 2025

Revised Date: 29 July 2025

Accepted Date: 9 September 2025

Please cite this article as: Capelli Ghioldi, G., Tamburello, G., Sciarra, A., Rouwet, D., Ricci, T., Civico, R., Tassi, F., Severi, P., Liuzzo, M., Coltorti, M., Rizzo, A.L., Methane seepage dynamics and ground heating phenomena in the southern Po Valley: the case study of Santa Maria Nuova (Italy), *Applied Geochemistry*, https://doi.org/10.1016/j.apgeochem.2025.106565.

Methane seepage dynamics and ground heating phenomena in the southern Po Valley: the case study of Santa Maria Nuova (Italy)

Capelli Ghioldi, G. [a,c]*, Tamburello, G.[a], Sciarra, A.[b], Rouwet, D.[a], Ricci, T.[b], Civico, R.[b], Tassi, F.[c], Severi, P. [d], Liuzzo, M.[e], Coltorti, M.[f], Rizzo, A. L.[g, h]

[a]*INGV, Istituto Nazionale di Geofisica e Vulcanologia, Sezione di Bologna, viale Berti Pichat 6/2, 40127, Bologna, Italy*

[b]*INGV, Istituto Nazionale di Geofisica e Vulcanologia, Sezione Roma 1, via di Vigna Murata, 605, 00143 Rome, Italy*

[c]*Department of Earth Sciences, University of Florence, Via G. La Pira 4, 50121 Firenze, Italy*

[d] *Geological, Soil and Seismic Area of the Emilia-Romagna Region, Viale Della Fiera 8, 40127, Bologna, Italy*

[e]*INGV, Istituto Nazionale di Geofisica e Vulcanologia, Sezione di Palermo, Via Ugo La Malfa 153, 90146, Palermo, Italy*

[f]*Department of Environmental Sciences and Prevention, University of Ferrara, via Saragat 1, 44122, Ferrara, Italy*

[g]*Department of Earth and Environmental Sciences, University of Milano-Bicocca, Milano, Italy*

[h]*INGV, Istituto Nazionale di Geofisica e Vulcanologia, Sezione di Milano, Via Alfonso Corti, 12, 20133, Milano, Italy*

* Corresponding author. Department of Earth Sciences, University of Florence, Via G. La Pira 4, 50121 Firenze (Italy). Tel: +39 3381555344 E-mail: gioia.capellighioldi@unifi.it

Submitted to Applied Geochemistry Journal

Highlights

- Localised CH_4 seepage, up to 917 g m^{-2} d^{-1}, identified within a 1.5 ha agricultural field.
- Isotopic data support a microbial origin of CH_4 from shallow carbonate deposits.
- Methanotrophic oxidation of seeped CH_4 leads to local CO_2 release and ground heating.
- RVI satellite data reveal persistent vegetation stress in the seepage zone since 2017.
- Field data from 2022-2023 confirm stable CH_4 emission patterns matching remote sensing anomalies.

Keywords: CH_4 seepage; sedimentary basins; microbial oxidation; soil heating; stable isotopes, RVI analysis

Abstract

Natural reservoirs that release CH_4 can substantially increase atmospheric greenhouse gas levels, posing environmental and safety risks. Degassing phenomena in the Emilia-Romagna region (Italy) have been documented across a variety of fluids and reservoir types, with a focus on their origin and evolution. This study combines ground measurements and satellite data analysis to explore the relationships between CH_4 seepage, thermal anomalies, and vegetation stress at the Santa Maria Nuova (SMN) site in southern Po Valley. The explosion of a CH_4-saturated water well in July 2021 prompted a two-year investigation in the adjacent cultivated field (1.5 ha), revealing significant spatial and temporal variations in diffuse CH_4 fluxes (ranging from 0 to 917 g m^{-2} d^{-1}) and corresponding CO_2 fluxes (1.9 to 466 g m^{-2} d^{-1}). Soil temperature measurements and thermal imaging identified localised ground heating, attributed to methanotrophic exothermic oxidation of CH_4 to CO_2. These hotspots correspond to areas of visibly stressed vegetation, marked by reduced vitality and barren areas. Satellite-derived Ratio Vegetation Index (RVI) data confirmed persistent vegetation stress over the anomaly site from 2017 to 2024. Geochemical analysis of soil gases indicated a primarily biogenic

origin of CH_4, supported by isotopic signatures ($\delta^{13}C$-CH_4 values < -60 ‰ V-PDB) and the presence of shallow Pleistocene carbonate deposits beneath the site, which can generate CH_4 seepage. These findings demonstrate the utility of integrating ground-based and remote sensing techniques for monitoring CH_4 seepage and its environmental impacts.

1. Introduction

Methane (CH_4) seepage refers to the release of natural gas from the subsurface into the surrounding environment. Methane-rich manifestations include onshore macro-seeps (such as mud volcanoes), submarine seepage, microseepage (as a diffusive flux from the soil), and thermal fluid discharges (Etiope et al., 2007a; 2009; Ricci et al., 2023). Around 53 Tg CH_4 y^{-1}, nearly 10% of the average global emission (EMEP/EEA 2023), are emitted from natural gas reservoirs into the atmosphere. However, due to the spatial and temporal heterogeneity of emissions, these estimates carry considerable uncertainty, as they rely on either bottom-up approaches or top-down modelling. Consequently, they are constrained by the extent of knowledge and the acquisition of direct measurements from geologically significant regions. A refined quantification of the geogenic CH_4 discharged into the atmosphere is crucial, as methane is a potent greenhouse gas with a global warming potential approximately 28-34 times higher than CO_2 over a 100-year period (IPCC, 2021). In addition to its role in climate change, atmospheric CH_4 affects tropospheric ozone formation and the oxidising capacity of the atmosphere. On a local scale, uncontrolled seepage of CH_4 and associated hydrocarbons may degrade air quality, alter soil microbial activity, and pose safety and environmental risks such as groundwater contamination and increased probability of explosions in confined spaces (Schout et al., 2020). Measurement of natural CH_4 emissions targets both diffusive degassing and punctual gas emissions, such as those from mud volcanoes and abandoned wells for hydrocarbon exploitation (e.g. Boothroyd et al., 2016).

Hydrocarbon-prone sedimentary basins host most macros and microseepages worldwide, which have long been used as indicators for potential oil or gas fields since the 1930s (Laubmeyer, 1933; Klusman, 1993; Tedesco, 1995; Abrams, 2005). In this environment, CH_4 is produced when organic matter buried within sediments undergoes biodegradation, carried out by microbial metabolic activity (biogenesis) and thermal alteration through cracking and reforming reactions caused by heat and pressure at depth (thermogenesis) (Schoell, 1980). Italy's methane reserves, currently totalling 37 billion cubic meters (ENI, 2023), result from Apennine orogenesis combined with Neogene tectonics and have been exploited for over a century, significantly reducing the surficial seepages (Etiope, 2009). In the Emilia-Romagna region (north-central Italy), historical records documented the occurrence of unusual events in several areas, such as gas bubbling, abrupt temperature increases in well water, rapid changes in the level of aquifer table, soil deformation and temperature increase, soil liquefaction, and the formation of sand and mud volcanoes (Capaccioni et al., 2015; Bonzi et al., 2017; Ricci et al., 2023). These phenomena have been observed concurrently with earthquakes (e.g., Sciarra et al., 2012), although without a clear spatiotemporal correlation pattern, while they also characterise periods of seismic quiescence (Sciarra et al., 2017). Active tectonics in sectors under compressive regimes are closely related to these gas seeps, as they promote the upward migration of gas by increasing pore pressure or creating new fractures, thereby enhancing permeability (Klusman, 1993; Etiope, 1999). Santa Maria Nuova Spallicci (hereafter referred to as SMN) is situated in the southeastern part of the Emilia-Romagna Region. In July 2021, a significant explosion was reported at this site, impacting a private water well. A spark from a water pump at the top of the well triggered the event. The rapid onset of a vigorous bubbling of CH_4-rich gases in the well water and a heavy metal panel at the well's exit created the conditions to rapidly exceed the lower flammability limit (4.4 vol% for CH_4) in the well and the subsequent explosion. During the survey in the following days, vigorous gas bubbling was still occurring, and non-dispersive infrared sensors placed at the wellhead revealed hazardous CH_4 levels (>5 vol%). The residents living in the neighbourhood reported the occurrence of numerous

95 microseepage events over the last decades, such as gas bubbles in ponds on the ground during heavy
96 rains or the interruption of construction work due to the presence of gas intercepted by excavations.
97 Close to the well lies an agricultural field cultivated with barley, which displayed circular barren
98 patches among the farming area. Similar surface manifestations have been observed in other areas of
99 the region, such as the Terre Calde di Medolla (Modena province), where vegetative distress has been
100 linked to diffuse gas emissions. In that area, CH_4 fluxes were found to drive methanotrophic oxidation,
101 resulting in elevated CO_2 emissions and localised soil heating, ultimately causing persistent vegetation
102 stress (Capaccioni et al., 2015; Sciarra et al., 2021). The explosion event, along with the presence of
103 anomalous vegetation patterns in the adjacent field, prompted a detailed investigation of gas seepage
104 dynamics at the SMN site, focusing on CH_4 and CO_2 emissions and the potential occurrence of
105 processes analogous to those documented at the Medolla site. Specifically, the research aims to (i)
106 quantify gas emissions employing ground-based measurements (i.e., accumulation chamber method),
107 (ii) characterise the origin of these emissions in terms of depth and production processes, (iii) propose
108 a method to identify potential sites where phenomena similar to those discussed in this paper may
109 occur, by analysing satellite-derived vegetation data.
110

111 **2. Study site**

112 SMN is in the Romagna Plain, approximately 8 km from the boundary with the Northern Apennines
113 (Fig. 1a). The ongoing evolution of the Northern Apennines into a fold-and-thrust belt since the
114 Cretaceous resulted from the collision between the European plate and the Adria microplate (Boccaletti
115 et al., 1971; Marroni et al., 2002). Tectonic pressures arising from the reciprocal approach of the Alps
116 and the Apennines, leading to a lowering in the central region, have generated the Po Valley. This vast
117 subsiding area forms a sedimentary basin primarily filled with marine sediments at its deepest point.
118 Alluvial sediments from rivers, including the Po River and its Alpine and Apennine tributaries,
119 contributed to surface sedimentation through flooding (Severi and Bonzi, 2014). In the Emilia-

Romagna plain, river-derived sediments are several hundred meters thick, overlaying coastal sediments and gradually transitioning to deeper and older marine deposits beneath. The geological units most affected by tectonic deformation are situated below those composing the deepest portion, buried by Plio-Pleistocene deposits (Capozzi and Picotti, 2002a). In the area including the study site, sandy-loamy alluvial deposits date back to the Roman and post-Roman periods (ISPRA, 2009), while in the subsurface, the alluvial deposits reach a depth of about 175 meters (Emilia-Romagna Region-ENI Agip, 1998). The latter covers basal Middle Pleistocene coastal marine sediments, followed by progressively older marine deposits. SMN is roughly halfway between two buried thrust faults located near the Apennine margin (Fig. 1b) and a bundle of buried thrust faults positioned closer to the sea, while 1.5 km upstream from SMN, there is a normal fault. The contour lines of the Pliocene base demonstrate the presence of a complex tectonic framework. Active tectonic structures corresponding to buried thrust fronts are present in the subsurface. Near SMN, earthquakes with $4 < M_W < 5.5$ having hypocentres at about 8 km have been recorded (Fig. 1b). In the Apennine foothills near Forlì, biogenic CH_4 emissions occur within deformed upper Neogene foredeep deposits (Capozzi and Picotti, 2002b). These units constitute an uplifted segment of the primary hydrocarbon system exploited in the eastern Po Plain (Mattavelli et al., 1983). These seepages are linked to biogenic CH_4 produced by degradation of Pliocene and Pleistocene organic-rich layers. It is plausible that a transitional border exists between a deeply buried zone of organic matter responsible for thermogenic CH_4 production and a shallowly buried zone where bacteria can still ferment the organic matter in the foredeep succession (Capozzi and Picotti, 2010).

3. Materials and Methods

3.1 Diffuse emissions of CH_4 and CO_2 from the soil and interstitial soil gases

Four seasonal field campaigns were conducted between May 2022 and October 2023 in the cultivated field at SMN to measure diffuse CH_4 and CO_2 fluxes from the soil. Flux measurements were carried

out approximately every six months, and each survey was completed within a single day of fieldwork, providing a representative snapshot of emission patterns under different seasonal conditions. Sampling points were distributed across an area of approximately 1.5 hectares, encompassing both zones with visible signs of vegetation stress and areas with normal vegetation cover. Locations with bare soil or sparse vegetation were generally easier to measure due to better surface accessibility. The spatial resolution varied between 75 and 130 measurement points per campaign, depending primarily on vegetation density and field accessibility. Gas flux measurements were carried out via the accumulation chamber method (Chiodini et al., 1998; Cardellini et al., 2003), using a portable West System™ flux meter equipped with a LICOR Li-820 infrared spectrophotometer for CO_2 and a tunable diode laser combined with a Herriott multipass cell for CH_4. The system operated with a Type B chamber, suitable for a wide range of fluxes. Measurement accuracy varies according to flux intensity: ±25% for fluxes between 1 and 1,500 mmol m^{-2} d^{-1}, and ±10% for fluxes between 1.5 and 300 mol m^{-2} d^{-1}, as specified by the manufacturer. The measured fluxes (as g m^{-2} d^{-1}) were processed through sequential Gaussian simulation (sGs) to extrapolate the values over a regular grid (5 x 5 meters). The sGs geostatistical method mitigates the smoothing effects produced by deterministic methods (e.g., ordinary Kriging) by generating multiple random realisations. In sGs, during the estimating procedure for each unknown point, both the estimates at the previously simulated sites and the actual values at sampled locations are considered (Deutsch and Journel, 1998). For every dataset, 200 simulations were produced and post-processed to construct CH_4 and CO_2 flux maps. The total output in t d^{-1} was computed based on the integration of the extrapolated fluxes over the entire area. Interstitial gas samples were collected where the gas flux and soil temperatures were anomalous (Fig. 2a). According to Tassi et al. (2015), soil gas was collected using a stainless-steel tube with an inner diameter of 4 mm at approximately 25 cm depth inserted into the soil and connected to a 100 mL syringe via a PTFE three-way valve used to fill a 1L air sampling bags (Supelco®). Both inorganic (O_2, N_2, CO_2) and organic (CH_4) gases were analysed at the Fluid Geochemistry Laboratory of INGV Rome by a

MicroGC Varian 4900, with an analytical error <3%. The isotopic carbon ratio of both CO_2 and CH_4 (expressed as $\delta^{13}C$-CO_2 and $\delta^{13}C$-CH_4, Vienna PeeDee Belemnite (VPDB) ‰) was determined via cavity ringdown spectroscopy (CDRS) with the Picarro G2201-i instrument, with a precision within 0.16 ‰ for $\delta^{13}C$–CO_2 and 1.15 ‰ for $\delta^{13}C$–CH_4.

3.2 Soil temperatures

To detect and characterise near-surface thermal anomalies potentially related to gas seepage, a multi-scale thermal survey was carried out. The September 2022 flux campaign was preceded by a drone-based thermal imaging survey using a DJI Matrice 300 UAV, equipped with a Zenmuse H20T radiometric thermal sensor, flown at 60 m above ground level. From that survey onward, each flux measurement campaign involved collecting soil temperature data at a depth of approximately 10 cm using a digital thermometer with a Type-K thermocouple of 20 cm. Thermal maps were also generated using the sGs method. Additionally, in 2024, a soil temperature station equipped with a Mini T1 datalogger and thermocouple was installed at the main anomaly spot at a depth of about 50 cm, from January to November. This dataset is included in the Supplementary Material (Fig. S1).

3.3 Vegetative cover and Sentinel-2 spectral data processing

After screening the area with Google Earth Pro to assess the temporal persistence of vegetation anomalies (Fig. 2b), these features were interpreted as a spatial indicator of CH_4 seepage in the field. The presence of a recurrent vegetation stress signal over several years supported its use as a preliminary guide for field investigations. These associations between plant stress, ground heating, and natural gas emissions, already demonstrated in the Terre Calde di Medolla site (Capaccioni et al., 2015; Sciarra et al., 2021), further strengthened their role as reliable indicators of subsurface gas migration. To corroborate the observations from the analysis of the satellite images, the cloud-based platform for geospatial analysis, Google Earth Engine (GEE, https://earthengine.google.com/), provided an

extensive database of satellite acquisitions that enabled spectral data processing. Specifically, the distinct spectral conditions of various vegetative covers can be identified by their overall ground elements: while leaf cellular structures strongly reflect near-infrared radiation (760-900 nm), visible radiation in the red (630-690 nm) is absorbed by chlorophyll (Tucker, 1979). Combining these two spectral domains makes it possible to distinguish plants from the soil and use vegetative cover density to calculate photosynthetically active biomass. The "Ratio Vegetation Index" (RVI), developed by Pearson and Miller (1972), enhances the contrast between the ground and vegetation:

$$RVI = NIR/R \quad (1)$$

Where R is the mean reflectance in the red channel, and NIR is the mean reflectance in the near-infrared channel. Considering this, the temporal trend of plant growth inhibition associated with gas seepage was evaluated by calculating the RVI of two different circular areas (~30 m radius) in the field: (1) one located in the central zone of the vegetative anomaly, where the ground was consistently bare or sparsely vegetated (RVI_{an}) and (2) one in a reference area with nominally healthy vegetation, used as background (RVI_{bg}). The selection of these areas was guided by the CH_4 flux maps obtained during the initial field campaigns, which helped to delineate zones of active seepage and unaffected vegetation. The Sentinel-2 spatial resolution for both spectral bands was 10 m, and the RVI was calculated considering the cloud coverage probability and excluding all R band values < 0.1, i.e. the cloud threshold value proposed by the sentinel2-cloud-detector library.

3.4 Groundwater monitoring at the exploded well

The exploded water well was equipped with an STS DL.WMS.BT.4G.LTC multi-parameter probe to continuously monitor potential signals of deep fluid migration. The probe includes a pressure sensor (0.05% full-scale accuracy), a temperature sensor (±0.1 °C), and a four-electrode electrical conductivity sensor with six titanium electrodes and a measurement error below 2.5% of the range.

Data were recorded at hourly intervals. The time series collected between June 2023 and December 2024 is presented and discussed in the Supplementary Material (Fig. S2).

4. Results

4.1 Diffuse gas emissions from the SMN field

Table 1 presents a statistical summary of CH_4 and CO_2 fluxes from the soil, along with the output estimates obtained from the sGs extrapolation, during the 2022-2023 campaigns. In May 2022, ΦCH_4 varied from 0 to 917 g m^{-2} d^{-1}, yielding a total estimated output of 0.82 ± 0.1 t d^{-1}. ΦCO_2 fluctuated between 28.2 and 308.5 g $m^{-2}d^{-1}$, leading to a total emission of 1.8 ± 0.18 t d^{-1}. By September 2022, CH_4 fluxes had significantly decreased, with values ranging from 0 to 5.8 g m^{-2} d^{-1} and a total output of 0.008 ± 0.003 t d^{-1}, while ΦCO_2 spanned from 9.4 to 174.8 g m^{-2} d^{-1}, with an output of 0.62 ± 0.05 t d^{-1}. The April 2023 campaign showed a new peak for CH_4, with fluxes up to 224.4 g m^{-2} d^{-1} and an estimated total output of 0.51 ± 0.09 t d^{-1}, whereas CO_2 fluxes ranged from 5.2 to 157.8 g m^{-2} d^{-1}, contributing to a total emission of 0.65 ± 0.07 t d^{-1}. Finally, in October 2023, CH_4 fluxes were once again low, ranging from 0 to 4.6 g m^{-2} d^{-1}, with a total output of 0.005 ± 0.002 t d^{-1}. CO_2 fluxes exhibited a broader range, from 1.9 to 466.1 g m^{-2} d^{-1}, with an overall emission of 0.66 ± 0.04 t d^{-1}. The spatial distributions of CH_4 and CO_2 fluxes, as derived from sGs interpolation, are shown in Fig. 3, where a permanent anomaly can be observed, particularly to the south of the agricultural field, throughout the two-year monitoring period.

4.2. Interstitial Soil Gases and Isotopic Data

The analytical results for interstitial gases collected in September 2022 and April 2023 are summarised in Table 2. CH_4 concentrations ranged from 0.00074% (22A) to 54.1% (23E), while CO_2 concentrations ranged from 0.07% (23A) to 6.88% (23D). The CH_4/CO_2 molar ratio spanned from 0.01 (22A) to 8.80 (23C), whereas O_2 content ranged between 4.7% (22B) to 20.03% (23F), and N_2

values varied from 37.6% (23E) to 78.7% (23A). The $\delta^{13}C$ values in CH_4 ranged from -61‰ V-PDB (22A) to -77.8‰ V-PDB (23E), while the $\delta^{13}C$-CO_2 values were from -52‰ V-PDB (23D) to -24‰ V-PDB (23C). These data are graphically represented in Figure 4, where panel (a) reports the $\delta^{13}C$ values of CH_4 and CO_2 for all samples, and panel (b) shows the CH_4/CO_2 molar ratio plotted against $\delta^{13}C$-CO_2.

4.3. Soil temperature measurements

The spatial distribution of ground surface temperatures obtained through both UAV-based thermal imaging and point-based measurements during the flux campaigns is shown in Fig. 5. Panel (a) shows the thermal orthomosaic acquired via drone prior to the September 2022 campaign. A warmer area is clearly visible in the southern-central sector of the cultivated field, where surface temperatures exceed 17 °C, contrasting with surrounding zones measuring as low as ~3 °C. Panels (b), (c), and (d) display soil temperature data collected at ~10 cm depth during the surveys conducted in September 2022, April 2023, and October 2023, respectively. In all three cases, a consistent temperature gradient is observed across the field, with relatively higher values located in the central-southern portion where vegetation appears sparser or absent. The temperature difference between warmer and cooler zones varies across the three campaigns: approximately 3 °C in September 2022 (panel b), up to 3.5 °C in April 2023 (panel c), and exceeding 10 °C in October 2023 (panel d). The more pronounced contrast visible in the UAV-derived dataset (panel a) is further addressed in the Discussion section.

4.4. RVI Analysis

The temporal evolution of the RVI calculated from Sentinel-2 satellite data for both the SMN and Medolla fields is shown in Fig. 6. The Medolla site is included in the analysis as it represents another location where vegetation stress has been documented in association with similar phenomena. At the Medolla site, the RVI_{an} was calculated over a larger anomaly area rather than a single point, capturing

a broader spatial impact. Both graphs cover the period from July 2017 to May 2024. At the SMN site (upper panel), RVI_{bg} values (green circles) exhibit a clear seasonal pattern, with sharp increases during the spring and early summer of each year. These peaks vary in magnitude, with particularly high values recorded in 2019 and again between 2022 and 2023. Notably, RVI_{bg} values show greater dispersion and variability compared to the RVI_{an} values. The RVI_{an} data (orange squares) display a lower amplitude of seasonal variation throughout the time series, with most values remaining below 4. The contrast between RVI_{an} and RVI_{bg} is especially marked during the peak growing seasons, when RVI_{bg} reaches its highest values, while RVI_{an} remains comparatively stable or only moderately increases. Dashed vertical lines indicate the four time points corresponding to the flux campaigns conducted in May 2022, September 2022, April 2023, and October 2023. At the Medolla site (lower panel), both RVI_{bg} and RVI_{an} show well-defined seasonal cycles, with elevated values during vegetative periods and lower values during the winter months. As at SMN, RVI_{bg} generally displays higher peaks than the corresponding RVI_{an}, although the two curves follow a more similar trend over time compared to SMN. Peak RVI_{bg} values often exceed 15 and reach up to ~25–27 in some years (notably in 2019 and 2020), whereas RVI_{an} values mostly remain below 15, even during peak growing seasons.

5. Discussion

5.1 Origin of gases

Methane in natural environments is mainly produced by two genetic processes, which can be distinguished using the carbon isotopic ratio of CH_4, expressed as $\delta^{13}C\text{-}CH_4$. Biogenic CH_4, mostly related to microbial activity in anoxic conditions, typically exhibits strongly depleted $\delta^{13}C$ values <-50 ‰ V-PDB, whereas thermogenic CH_4, formed from the thermal decomposition of organic matter at high temperatures, shows less negative $\delta^{13}C$ values ranging from -50‰ to -30‰ V-PDB (Schoell, 1980; Whiticar, 1999). However, these isotopic signatures should be considered indicative rather than definitive, as overlaps can occur due to secondary processes such as fractionation or mixing of gases

from different origins (Mattavelli & Novelli, 1983), especially in complex geological settings. The isotopic analysis of SMN soil gases reveals a distinctly biogenic origin, with all δ^{13}C-CH_4 values below -60 ‰ V-PDB (Table 2). Figure 4a illustrates the relationship between δ^{13}C-CH_4 and δ^{13}C-CO_2, contextualised within the genetic fields and isotopic processes defined by Milkov and Etiope (2018). The isotopic composition of soil gases from the SMN site falls within the CO_2 reduction (CR) field, indicating that CH_4 is primarily generated through microbial carbonate reduction in marine sediments. This pathway favours the production of ^{12}C-enriched CH_4, which is consistent with the characteristics of CH_4 emissions in the area (Tassi et al., 2012). The δ^{13}C-CO_2 values of the soil samples also provide further insights that point to other methane-related processes. While approximately half of the samples display $^{13}C/^{12}C$ ratio values typical of CO_2 sources linked to soil respiration and organic matter decomposition (e.g. -20‰ to -30‰ V-PDB; Amundson et al., 1998), others exhibit significantly depleted δ^{13}C-CO_2 values (e.g., 23D: -52‰, 23E: -37‰, 23A: -39‰). Such highly negative values suggest an enhanced influence of methanotrophic activity, where the microbial oxidation of CH_4 results in the transfer of the δ^{13}C-CH_4 signature to CO_2 through isotopic mass balance, ^{12}C being preferentially incorporated into the oxidised CO_2. Although some degree of atmospheric contamination may affect the δ^{13}C values in certain samples (particularly in sample 22A, which is characterised by low CO_2 concentrations and roughly atmospheric N_2 and O_2 values), the overall isotopic signatures remain consistently depleted in ^{13}C. This suggests that atmospheric dilution has a limited impact on the measured isotopic composition of both gases and does not significantly bias the interpretation of their origin. Figure 4b further supports this interpretation by showing the relationship between δ^{13}C-CH_4 and the CH_4/CO_2 ratio. The observed trend indicates that as CH_4/CO_2 decreases, δ^{13}C-CH_4 becomes progressively enriched in ^{13}C. For comparison, Fig. 4b also includes gas data from the Terre Calde di Medolla site, sourced from Capaccioni et al. (2015). Despite variations in sampling depth, these data exhibit a similar trend of increasing δ^{13}C-CH_4 values with decreasing CH_4/CO_2 ratios. The extent of CH_4 oxidation, however, is likely influenced by several environmental factors, including

oxygen availability, temperature, soil moisture, microbial community density, soil composition, land use, and vegetation cover (Shukla et al., 2013). This interpretation aligns with the general characteristics of gas reservoirs in the Padania Plain and the southern Po River Basin, where CH_4 is generated at relatively shallow depths (1.5–2 km) and lower temperatures (~50°C) within the Pliocene-Pleistocene sedimentary infill of the Apennine Chain foredeep (Martinelli et al., 2012; Ricci et al., 2023). These microbial gas accumulations contrast with the thermogenic CH_4 found in the Emilian sector of the Apennines, west of the study area, where gas emissions display a clear thermogenic signature associated with deeper and higher-temperature formations (Tassi et al., 2012). The geological cross-section in Fig. 7 (trace shown in Fig. 1b) reveals that the marine deposits of Pliocene to Pleistocene age beneath the study area are less than 0.5 km thick. These sediments, consisting of alluvial gravel and sand with interbedded clay, directly overlie Messinian clay–sand alternations, as documented in the Cannuzzuola I well log (available at www.videpi.com). Given that microbial carbonate reduction typically occurs in shallow, organic-rich marine sediments, the Pliocene–Pleistocene layers represent a plausible domain for bacterial CH_4 generation. The underlying evaporitic sequence is considered an unlikely host for organic matter. Instead, a deeper gas source could be associated with the Marnoso-Arenacea turbidite formation, which lies at depths exceeding 1 km. However, CH_4 from this unit, as reported by Mattavelli et al. (1983), is of mixed biogenic and thermogenic origin and typically exhibits a heavier carbon isotopic signature than that observed in our samples. Moreover, the cross-section highlights two reverse faults intersecting the stratigraphic succession. These tectonic structures may act as preferential pathways for the upward migration of gas, supporting the hypothesis that fault-controlled permeability plays a key role in channelling the emissions observed at the surface.

5.2 Spatial and temporal evolution of ΦCH_4 and ΦCO_2

The spatial distribution maps of the CH_4 soil fluxes reveal a confined area, located south of the agricultural field, of significant anomaly consistently detected throughout the two-year surveys (Fig. 3). During both spring campaigns (May 2022 and April 2023), the main CH4 anomaly was consistently accompanied by a secondary flux anomaly located slightly to the west, an additional feature that was absent in the autumn surveys. Notably, CH_4 fluxes measured in spring reached values up to two orders of magnitude higher than those recorded in autumn. This recurring pattern suggests a potential seasonal control on CH_4 seepage. Various factors could drive this seasonality, with soil moisture playing a key role by influencing soil permeability and gas transport pathways. However, further targeted investigations are necessary to clarify the mechanisms underlying this seasonal variability. According to the Etiope and Klusman (2010) classification, high CH_4 microseepage is defined as fluxes greater than 50 mg m^{-2} d^{-1}, medium microseepage ranges from 5 to 50 mg m^{-2} d^{-1}, and low microseepage is from 0 to 5 mg m^{-2} d^{-1}. At SMN, many CH_4 fluxes vastly exceeded the high microseepage range (Table 1), even when environmental factors inhibit the flux. The spatial distribution of ΦCO_2 mirrored that of ΦCH_4 (Fig. 3), consistent with both gases being produced and consumed by microbial activity. This pattern aligns with previous studies in the Terre Calde di Medolla area (Capaccioni et al., 2015), which documented a strong correlation between CH_4 and CO_2 fluxes at sites dominated by microbial gas generation and oxidation processes. Typical biogenic soil respiration fluxes of CO_2 in similar environments, in the absence of additional sources, generally reach several tens of g m^{-2} d^{-1} (Chiodini et al., 2008). In the anomalous spots of the study area, the observed ΦCO_2 values exceed these background levels, indicating a significant contribution from methanotrophy. To quantify the relative contribution of CH_4 oxidation and background soil respiration to total CO_2 flux, the distribution of September 2022 CO_2 flux values was modelled using a Gaussian Mixture Model (GMM), applying the Expectation-Maximisation (EM) algorithm to fit a finite model representing two normal populations of the empirical distribution. This statistical decomposition enabled the estimation of the mean and mixing fraction of each population (Fig. 8). The lower CO_2 flux population, which is the

most common, represents background soil respiration and is observed across both areas with and without CH_4 anomalies. This population accounted for 69% of the total flux, while the population associated with CH_4 oxidation contributed the remaining 31%. The mean and standard deviation of these two components were used in a Monte Carlo simulation with 3,000 iterations to estimate the mean flux and associated uncertainty for each population. The results indicated flux values of 143.2 ± 26.5 g CO_2 m^{-2} d^{-1} for the CH_4 oxidation population and 36.7 ± 2.7 g CO_2 m^{-2} d^{-1} for the background soil respiration population.

5.3 Thermal Anomaly and Vegetation Health Assessment

A significant discrepancy in the recorded temperature ranges emerges between thermal maps derived from drone-based imaging and those obtained from ground-based measurements (Fig. 5). This is primarily due to the nature of the measurements since drone imaging captures the surface temperature, while the other maps represent soil temperature at a depth of 15 cm. Additionally, the thermal emissivity coefficient (ε) is uniformly applied to the entire acquisition, disregarding the presence of materials different from the soil (e.g., cement, metal from orchard fences). Despite the thermal maps not being directly comparable, this approach enables the identification of thermal anomalies while providing spatial continuity for the temperature parameter observed across various time intervals. The highest temperatures were consistently measured at and around the main CH_4 emission spot, even across time (Fig. S2), where the exothermic oxidation of CH_4 to CO_2 generates localised heating (Capaccioni et al., 2015). Seasonal variations in ground temperature and soil moisture modulate the extent and intensity of this thermal anomaly since these environmental factors influence gas mobility and microbial growth in the soil. Furthermore, the release of CH_4 and subsequent oxidation into CO_2 by methanotrophic bacteria affect plant health, often leading to a charred appearance and irregular, thinning growth near the gas leaks (Davis, 1977). These stress responses are further compounded by

changes in nutrient cycling and microbial competition, which can reduce nitrogen availability essential for plant development (Karbin et al., 2015; Chang et al., 2024). The observed oxygen depletion in three interstitial gas soil samples (22B, 23D, 23E) also indicates that oxidative methane processes could impair root respiration. The adverse effects on vegetation are reflected in the RVI time series at SMN (Fig. 6), which shows consistently lower values at the anomaly spot compared to the surrounding areas. The seasonal RVI fluctuations (higher in spring and summer, lower in fall and winter) indicate regular vegetation cycles in unaffected regions. In contrast, the anomaly spot exhibits suppressed growth, reinforcing the hypothesis that CH_4 emissions negatively impact plant health. This difference in vegetation vitality is captured through satellite-derived spectral reflectance data. Typically, an RVI < 1 signals significant vegetation stress or sparse cover due to lower NIR reflectance relative to Red light (Richardson and Wiegand, 1977). However, despite expected distress from gas seepage, the anomaly (RVI_{an}) remains above this threshold, likely due to the 10m resolution of Sentinel-2, which averages localised effects over a broader area, thus diluting the visible impact on vegetation. Other factors may also influence RVI, including the phenological stage, where young or senescing plants exhibit different reflectance from mature vegetation (Kobayashi et al., 2018). Additionally, the crop rotation (i.e., barley cultivation in 2022 and fava bean in 2024) introduces species with distinct spectral characteristics due to differences in leaf structure and water content, further altering the RVI. Soil moisture and background reflectance are also essential; moist soils reduce NIR reflectance, while dry soils increase it, potentially lowering RVI values (Polivova et al., 2022). A direct comparison of the SMN and Medolla RVI time series enhances understanding of how vegetation responds to gas-related stress under various site conditions. At both sites, the anomaly RVI consistently shows lower values than the surrounding background RVI, indicating persistent reduction in vegetation vitality near the gas seepage areas. However, the RVI_{bg}–RVI_{an} gap is notably wider at SMN (especially evident during the growing seasons), suggesting more intense or sustained stress. In contrast, the Medolla site exhibits more robust vegetation growth overall, with higher and sharper RVI peaks, even at the anomaly

location, implying either less severe environmental stress or more favourable baseline conditions. The more pronounced vegetation decline at SMN could be linked to chronic exposure to CH_4 emissions, whereas the stress at Medolla may be more episodic or buffered by local factors such as soil composition, land management, or microclimatic conditions.

6. Conclusions

The study investigated the spatial and temporal variability of CH_4 microseepage and associated ground heating phenomena at SMN site, in northern Italy. Seasonal gas flux monitoring revealed that methane emissions can vary by up to three orders of magnitude, with peak fluxes typically occurring in spring. The CH_4 seepage is attributed to microbial generation in shallow marine carbonate-rich sediments, consistent with other known seepage systems in the Po Plain. The observed ground heating, likely linked to exothermic methanotrophic oxidation, is associated with inhibited vegetation growth at the seepage site. Long-term satellite observations support the persistence of these effects over multiple years. Future studies could expand on these findings by incorporating vegetation stress indicators, such as chlorophyll content or spectral indices, to better quantify the impact of soil heating on plant health. Additionally, stable isotope analysis of plant tissues or rhizosphere gases could help refine the understanding of methane–biosphere interactions at these seepage sites.

Acknowledgements

This research was funded by the IDRO-Nord project, part of the Progetto Centro Italia DL50 – Reti Idrogeochimiche, of the Istituto Nazionale di Geofisica e Vulcanologia. The researchers sincerely thank Matteo, the owner of the agricultural field, for his constant availability and support in allowing us to conduct our research. We sincerely thank the Editor and the reviewers for their valuable corrections and insightful comments, which significantly improved the quality of this manuscript.

CRedit Author Statement

G. Capelli Ghioldi: Writing – original draft, Conceptualisation, Visualisation, Validation, Formal analysis, Methodology, Investigation, Resources, Data Curation. **G. Tamburello**: Writing – original draft, Conceptualisation, Methodology, Software, Formal analysis, Investigation, Resources, Data Curation, Supervision, Project administration. **A. Sciarra**: Writing – review & editing, Methodology, Validation, Investigation, Resources. **D. Rouwet**: Writing – review & editing, Methodology, Validation, Investigation, Resources. **T. Ricci**: Writing – review & editing, Methodology, Validation, Investigation, Resources. **R. Civico**: Writing – review & editing, Methodology, Validation, Investigation, Resources. **F. Tassi**: Writing – review & editing, Supervision, Validation, Resources. **P. Severi**: Writing – review & editing, Methodology, Investigation, Resources. **M. Liuzzo**: Writing – review & editing, Methodology, Validation, Investigation, Resources. **M. Coltorti**: Writing – review & editing, Methodology, Investigation, Resources. **A.L. Rizzo**: Writing – review & editing, Validation.

Declaration of Competing Interest

The authors declare that they have no known competing financial interests or personal relationships that could have appeared to influence the work reported in this paper.

References

Abrams, M.A., 2005. Significance of hydrocarbon seepage relative to petroleum generation and entrapment. Mar. Pet. Geol. 22, 457–477.

Amundson, R., Stern, L., Baisden, T., Wang, Y., 1998. The isotopic composition of soil and soil-respired CO_2. Geoderma, Volume 82, Issues 1–3, 83-114, https://doi.org/10.1016/S0016-7061(97)00098-0

Boccaletti, M., Elter, P., Guazzone, G., 1971. Plate tectonics models for the development of the western Alps and northern Apennines. Nature 234, 108–111

Bonzi, L., Ferrari, V., Martinelli, G., Norelli, E., & Severi, P., 2017. Unusual geological phenomena in the Emilia-Romagna plain (Italy): Gas emissions from wells and the ground, hot water wells, geomorphological variations. A review and an update of documented reports. Bollettino Di Geofisica Teorica Ed Applicata, 58(2), 87–102. https://doi.org/10.4430/bgta0193

Boothroyd, I.M., Almond, S., Qassim, S.M., Worrall, F., Davies, R.J., 2016. Fugitive emissions of methane from abandoned, decommissioned oil and gas wells. Science of the Total Environment 547, 461-469. https://doi.org/10.1016/j.scitotenv.2015.12.096

Capaccioni, B., Tassi, F., Cremonini, S., Sciarra, A., Vaselli, O., 2015. Ground heating and methane oxidation processes at shallow depth in Terre Calde di Medolla (Italy): observations and conceptual model. J. Geophys. Res. Solid Earth 120, 3048–3064. https://doi.org/10.1002/2014JB011635.

Capozzi, R., & Picotti, V., 2002a. Fluid migration and origin of a mud volcano in the Northern Apennines (Italy): The role of deeply rooted normal faults. Terra Nova, 14(5), 363–370. https://doi.org/10.1046/j.1365-3121.2002.00430.x

Capozzi, R., & Picotti, V., 2002b. Pliocene sequence stratigraphy, climatic trends and sapropel formation in the Northern Apennines (Italy). Palaeogeography, Palaeoclimatology, Palaeoecology, Volume 190, 2003. 349-371. https://doi.org/10.1016/S0031-0182(02)00614-4

Capozzi, R., & Picotti, V., 2010. Spontaneous fluid emissions in the Northern Apennines: Geochemistry, structures and implications for the petroleum system. Geological Society Special Publication, 348, 115–135. https://doi.org/10.1144/SP348.7

Cardellini, C., Chiodini, G., Frondini, F., 2003. Application of stochastic simulation to CO2 flux from soil: mapping and quantification of gas release. J. Geophys. Res. 108, 2425 https://doi.org/10.1029/2002JB002165

Chiodini, G., Cioni, R., Guidi, M., Raco, B., Marini, L., 1998. Soil CO2 flux measurements in volcanic and geothermal areas. Appl. Geochem. 13, 543–552. https://doi.org/10.1016/S0883-2927(97)00076-0

Chiodini, G., Caliro, S., Cardellini, C., Avino, R., Granieri, D., Schmidt, A., 2008. Carbon isotopic composition of soil CO2 efflux, a powerful method to discriminate different sources feeding soil CO2 degassing in volcanic-hydrothermal areas. Earth Planet. Sci. Lett. 274, 372–379. https://doi.org/10.1016/j.epsl.2008.07.051

Davis, S. H., 1977. The effect of natural gas on trees and other vegetation. Arboriculture & Urban Forestry (AUF), 3(8), 153-154. https://doi.org/10.48044/jauf.1977.039

Deutsch, C.V., and Journel, A.G., 1998. GSLIB: Geostatistical Software Library and Users Guide. Oxford Univerity Press, New York (369 pp.)

EMEP-EEA, 2023. Geological seepage – B1109. Natural Sources. EMEP/EEA Air Pollutant Emission Inventory Guidebook – 2023 – Chapter 11. Technical Guidance to Prepare National Emission Inventories. EEA Technical Report N° 6/2023. European Environment Agency, Copenhagen. https://doi.org/doi/10.2800/795737

Etiope, G., 1999. Subsoil CO_2, and CH_4 and their advective transfer from faulted grassland to the atmosphere. J. Geophys. Res. 104 (D14), 16,889. https://doi.org/10.1029/1999JD900299

Etiope, G., Fridriksson, T., Italiano, F., Winiwarter, W., Theloke, J., 2007a. Natural emissions of methane from geothermal and volcanic sources in Europe. J. Volcanol. Geoth. Res., 165, 76–86. https://doi.org/10.1016/j.jvolgeores.2007.04.014

Etiope, G., Martinelli, G., Caracausi, A., and Italiano, F., 2007b. Methane seeps and mud volcanoes in Italy: Gas origin, fractionation and emission to the atmosphere, Geophys. Res. Lett., 34, L14303, https://doi.org/10.1029/2007GL030341

Etiope, G., 2009. Natural emissions of methane from geological seepage in Europe. Atmos. Environ. 43, 1430–1443. https://doi.org/10.1016/j.atmosenv.2008.03.014.

Etiope, G., & Klusman, R. W., 2010. Methane microseepage in drylands: soil is not always a CH4 sink. Journal of Integrative Environmental Sciences, 7(sup1), 31–38. https://doi.org/10.1080/19438151003621359

538 Etiope, G., and Schwietzke, S., 2019. Global geological methane emissions: An update of top-down
539 and bottom-up estimates. Elem Sci Anth, 7: 47. https://doi.org/10.1525/elementa.383
540
541 IPCC, 2021. Climate Change 2021: The Physical Science Basis. Contribution of Working Group I to
542 the Sixth Assessment Report of the Intergovernmental Panel on Climate Change [Masson-Delmotte,
543 V., Zhai, P., Pirani, A., Connors, S.L., Péan, C., Berger, S., Caud, N., Chen, Y., Goldfarb, L., Gomis,
544 M.I., Huang, M., Leitzell, K., Lonnoy, E., Matthews, J.B.R., Maycock, T.K., Waterfield, T., Yelekçi,
545 O., Yu, R., and Zhou, B. (eds.)]. Cambridge University Press, Cambridge, United Kingdom and New
546 York, NY, USA, 2391 pp. https://doi.org/10.1017/9781009157896
547
548 ISPRA, 2009. Note illustrative della Carta Geologica d'Italia Foglio n. 255 Cesena e Fogli 240-241
549 Forlì – Cervia (2005).
550
551 Klusman, R.W., 1993. Soil Gas and Related Methods for Natural Resource Exploration. J. Wiley &
552 Sons, Chichester, U.K. 483 pp.
553
554 Kobayashi, H., Nagai, S., Kim, Y., Yang, W., Ikeda, K., Ikawa, H., Nagano, H., Suzuki, R., 2018. In
555 Situ Observations Reveal How Spectral Reflectance Responds to Growing Season Phenology of an
556 Open Evergreen Forest in Alaska. Remote Sens. 10, 1071. https://doi.org/10.3390/rs10071071
557
558 Laubmeyer, G., 1933. A New Geophysical Prospecting Method, Especially for Deposits of
559 Hydrocarbons: Petrol. London, vol. 29, p. 14.
560

561 Marroni, M., Molli, G., Montanini, A., Ottria, G., Pandolfi, L., Tribuzio, R., 2002. The external
562 Ligurian units (Northern Apennine, Italy): from rifting to convergence of a fossil ocean-continent
563 transition zone. Ofioliti 27:119–131 https://doi.org/10.4454/ofioliti.v27i2.182
564
565 Martinelli, G., Cremonini, S., Samonati, E., 2012. Geological and geochemical setting of natural
566 hydrocarbon emissions in Italy. In: Al-Megren H (ed) Advances in Natural Gas Technology. InTech,
567 London
568
569 Mattavelli, L., Ricchiuto, T., Grignani, D., and Schoell, M. (1983). Geochemistry and habitat of natural
570 gases in Po basin, Northern Italy. AAPG bulletin, 67(12), 2239-2254.
571 https://doi.org/10.1306/AD46094F-16F7-11D7-8645000102C1865D
572
573 Milkov, A. V., Etiope, G., 2018. Revised genetic diagrams for natural gases based on a global dataset
574 of >20,000 samples. Organic Geochemistry, Volume 125, Pages 109-120, ISSN 0146-6380.
575 https://doi.org/10.1016/j.orggeochem.2018.09.002
576
577 Pearson, R. L. and Miller, L. D., 1972. Remote mapping of standing crop biomass for estimation of
578 the productivity of the shortgrass prairie, Pawnee National Grasslands, Colorado. Proceedings of the
579 8th International Symposium on Remote Sensing of the Environment II: 1355–1379.
580
581 Pignone, R., Cibin, U., Severi, P., Roveri, M., Correggiari, A., Trincardi, F., Preti, D., 2001. Carta
582 geologica d'Italia. Scala 1:50.000, Foglio 240 – Forlì. CARG
583

584 Polivova, M., and Brook, A., 2022. Detailed Investigation of Spectral Vegetation Indices for Fine
585 Field-Scale Phenotyping. Vegetation Index and Dynamics, IntechOpen, Crossref,
586 http://dx.doi.org/10.5772/intechopen.96882
587
588 Regione Emilia-Romagna, ENI - AGIP, 1998. Riserve idriche sotterranee della Regione Emilia-
589 Romagna. A cura di G. Di Dio. S.EL.CA. (Firenze), 120 pp.
590
591 Ricci, A., Cremonini, S., Severi, P., Tassi, F., Vaselli, O., Rizzo, A. L., Caracausi, A., Grassa, F.,
592 Fiebig, J., Capaccioni, B., 2023. Sources and migration pathways of methane and light hydrocarbons
593 in the subsurface of the Southern Po River Basin (Northern Italy). Marine and Petroleum Geology,
594 147. https://doi.org/10.1016/j.marpetgeo.2022.105981
595
596 Richardson, A.J., Wiegand, C.L., 1977. Distinguishing vegetation from soil background information.
597 Photogramm. Eng. Rem. S. 43(12), 1541-1552.
598
599 Severi, P., Bonzi, L., 2014. Esperienze e prospettive nel monitoraggio delle acque sotterranee. Il
600 contributo dell'Emilia-Romagna, cured by Farina, M., Marcaccio, M., Zavatti, A. Chapter 2. Pitagora
601 Editrice Bologna
602
603 Schoell, M., 1980. The hydrogen and carbon isotopic composition of methane from natural gases of
604 various origins. Geochim. Cosmochim. Acta, 44, 649–661. https://doi.org/10.1016/0016-
605 7037(80)90155-6
606

607 Schout, G., Hartog, N., Hassanizadeh, S. M., Helmig, R., & Griffioen, J., 2020. Impact of groundwater
608 flow on methane gas migration and retention in unconsolidated aquifers. Journal of Contaminant
609 Hydrology, 230. https://doi.org/10.1016/j.jconhyd.2020.103619
610
611 Sciarra, A., Cantucci, B., Buttinelli, M., Galli, G., Nazzari, M., Pizzino, L., Quattrocchi, F., 2012. Soil-
612 gas survey of liquefaction and collapsed caves during the Emilia seismic sequence. Annals of
613 Geophysics, 55(4). https://doi.org/10.4401/ag-6122
614
615 Sciarra, A., Cantucci, B., & Coltorti, M., 2017. Learning from soil gas change and isotopic signatures
616 during the 2012 Emilia seismic sequence. Scientific Reports, 7(1). https://doi.org/10.1038/s41598-
617 017-14500-y
618
619 Sciarra, A., Cantucci, B., Sapia, V., De Ritis, R., Ricci, T., Civico, R., Galli, G., Cinti, D., Coltorti,
620 M., 2021. Geochemical and geoelectrical characterization of the Terre Calde di Medolla (Emilia-
621 Romagna, northern Italy) and relations with 2012 seismic sequence. J. Geochem. Explor. 221, 106678.
622 https://doi.org/10.1016/j.gexplo.2020.106678.
623
624 Tassi, F., Bonini, M., Montegrossi, G., Capecchiacci, F., Capaccioni, B., Vaselli, O., 2012. Origin of
625 light hydrocarbons in gases from mud volcanoes and CH_4-rich emissions. Chemical Geology, Volumes
626 294–295, Pages 113-126, ISSN 0009-2541. https://doi.org/10.1016/j.chemgeo.2011.12.004.
627
628 Tassi, F., Venturi, S., Cabassi, J., Capecchiacci, F., Nisi, B., Vaselli, O., 2015. Volatile organic
629 compounds (VOCs) in soil gases from Solfatara crater (Campi Flegrei, southern Italy): Geogenic
630 source(s) vs. biogeochemical processes. Applied Geochemistry, Volume 56, Pages 37-49.
631 https://doi.org/10.1016/j.apgeochem.2015.02.005

Tedesco, S.A., 1995. Surface Geochemistry in Petroleum Exploration. Chapman & Hall, New York. 206 pp.

Tucker, C.J., 1979. Red and Photographic Infrared Linear Combinations for Monitoring Vegetation. Remote Sensing of the Environment 8:127-150. https://doi.org/10.1016/0034-4257(79)90013-0

Whiticar, M. J., 1999. Carbon and hydrogen isotope systematics of bacterial formation and oxidation of methane. Chem. Geol., 161, 291–314. https://doi.org/10.1016/S0009-2541(99)00092-3

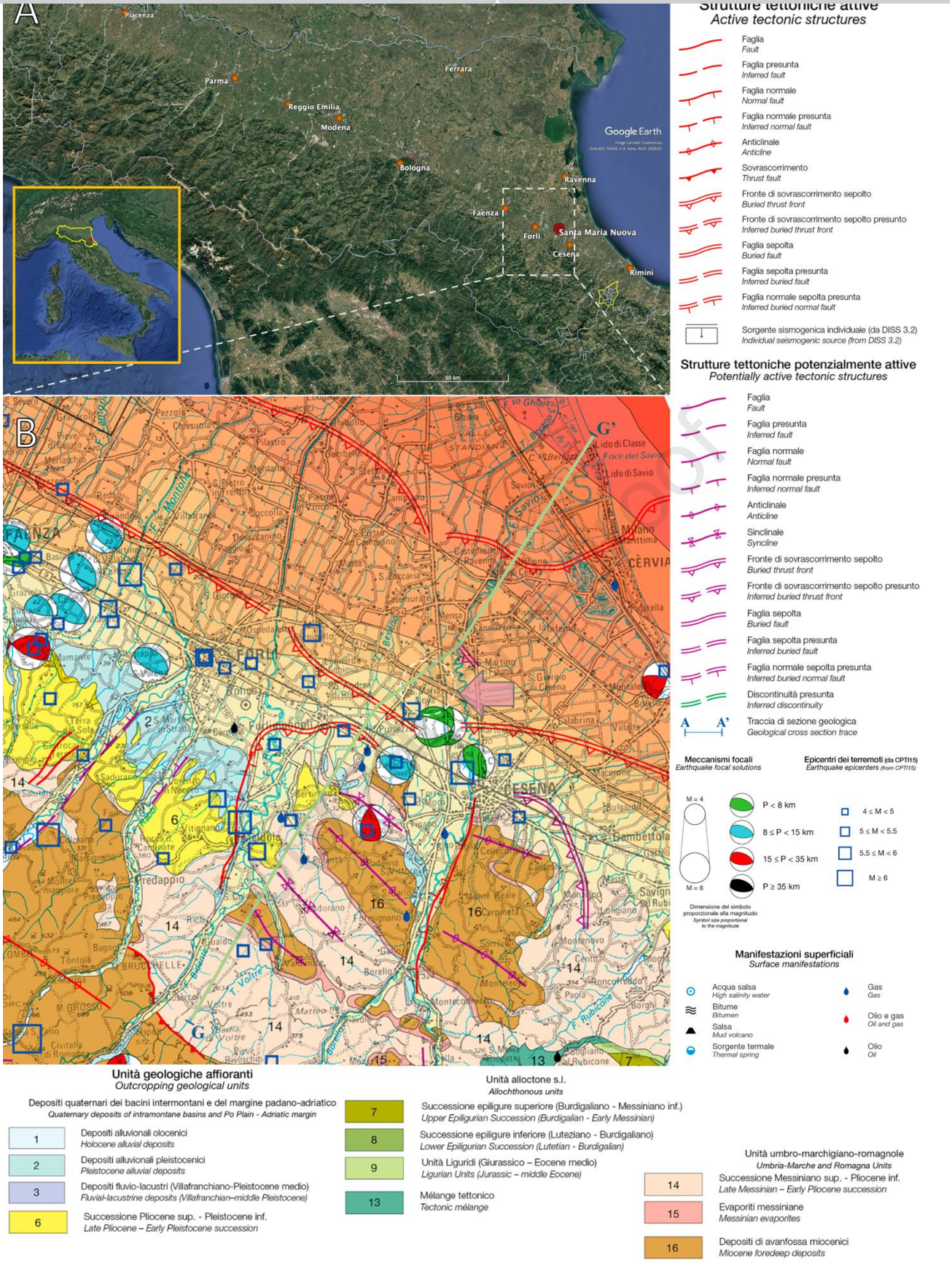

Figure 1. Regional setting of the study area. (a) Satellite image of the Emilia-Romagna region (Google Earth) and its main cities, illustrating the location of the Santa Maria Nuova site (red circle). The grey dashed box corresponds to the detailed seismotectonic map (b), which displays the primary tectonic structures and geological formations in the vicinity of SMN (indicated by the pink arrow and encircled in white), the locations of earthquakes along with their magnitude and depth, as well as reports of hydrocarbon manifestations, including a trace of geological cross-section G-G' (highlighted in green)

that passes over the site (Emilia-Romagna Region; 2016). To view the complete map, please consult https://mappegis.regione.emilia-romagna.it/gstatico/documenti/sismotett_2016/Carta_Sismotettonica.pdf.

Figure 2. (a) Aerial view of the SMN field and surrounding area. The yellow dashed line outlines the cultivated field where gas flux measurements were conducted. The red circle shows the location of the CH_4 saturated well, and orange triangles indicate the sampling points for interstitial gas. (b) A time series of satellite photographs (Google Earth) of the field emphasising the persistence of the anomaly in the vegetation.

ΦCH$_4$ (g m^{-2} d^{-1})

	Value Range	Mean	Median	Standard Deviation	Output in t d^{-1}
May 2022	0 – 916.9	25.3	11.6	51.3	0.82 ± 0.1
September 2022	0 – 5.8	0.5	0.4	0.4	0.008 ± 0.003
April 2023	0 – 224.4	28.2	18.1	31.7	0.51 ± 0.09
October 2023	0 – 4.6	0.4	0.2	0.5	0.005 ± 0.002

ΦCO$_2$ (g m^{-2} d^{-1})

	Value Range	Mean	Median	Standard Deviation	Output in t d^{-1}
May 2022	28.2 - 308.5	73.8	63.8	35.8	1.8 ± 0.18
September 2022	9.4 - 174.8	42.4	35.8	24.3	0.62 ± 0.05
April 2023	5.2 - 157.8	37.2	31.7	24.2	0.65 ± 0.07
October 2023	1.9 – 466.1	43.9	26.3	48.3	0.66 ± 0.04

Table 1. Descriptive statistics of the soil diffuse CH_4 and CO_2 flux values for the 2022-2023 surveys (in g m^{-2} d^{-1}) and total output in t d^{-1}.

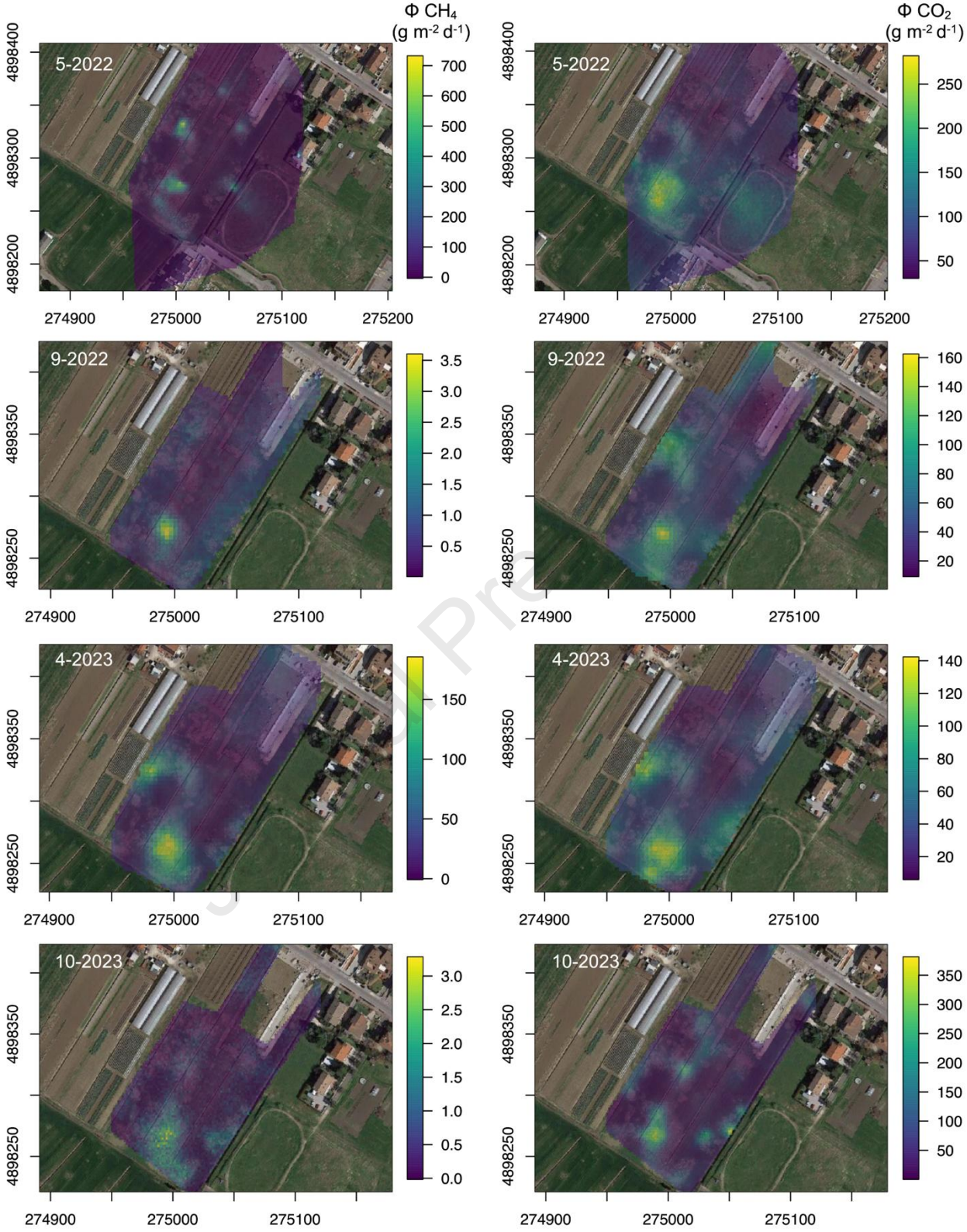

Figure 3. Flux distribution of CH_4 and CO_2 at the SMN Site during the 2022-2023 observation period. Both flux measurements were processed using a Sequential Gaussian Simulation and are expressed in g m^{-2} d^{-1}.

ID	Date	O_2 vol %	N_2 vol %	CH_4 vol %	CO_2 vol %	CH_4/CO_2	$\delta^{13}C$-CH_4 ‰ V-PDB	$\delta^{13}C$-CO_2 ‰ V-PDB
22A	2022/09/23	19.7	75.5	0.00074	0.09	0.01	-61	-25
22B	2022/09/23	4.7	61.7	29.78	6.43	4.63	-74.5	-30
23A	2023/04/04	19.99	78.71	0.95	0.07	13.57	-72	-26
23A*	2023/04/04	19.99	77.65	1.03	0.09	11.44	-68	-39
23B	2023/04/04	17.73	72.57	7.05	1.23	5.73	-69	-35
23C	2023/04/04	17.74	72.14	7.74	0.88	8.80	-76	-24
23D	2023/04/04	8.25	59.29	25.57	6.88	3.72	-68	-52
23E	2023/04/04	6.07	37.61	54.08	2.69	20.10	-77.8	-37
23F	2023/04/04	20.03	78.32	0.01	0.15	0.07	-72	-

691
692
693 Table 2. Displays the sample ID, date, depth, chemical composition in vol%, and the CH_4/CO_2 ratio, along with the isotopic
694 carbon ratios of CO_2 and CH_4 expressed as $\delta^{13}C$ ‰V-PDB for the interstitial gases at the SMN field. The analysis for
695 sample 23A* relates to a slightly greater depth of 35 cm.
696

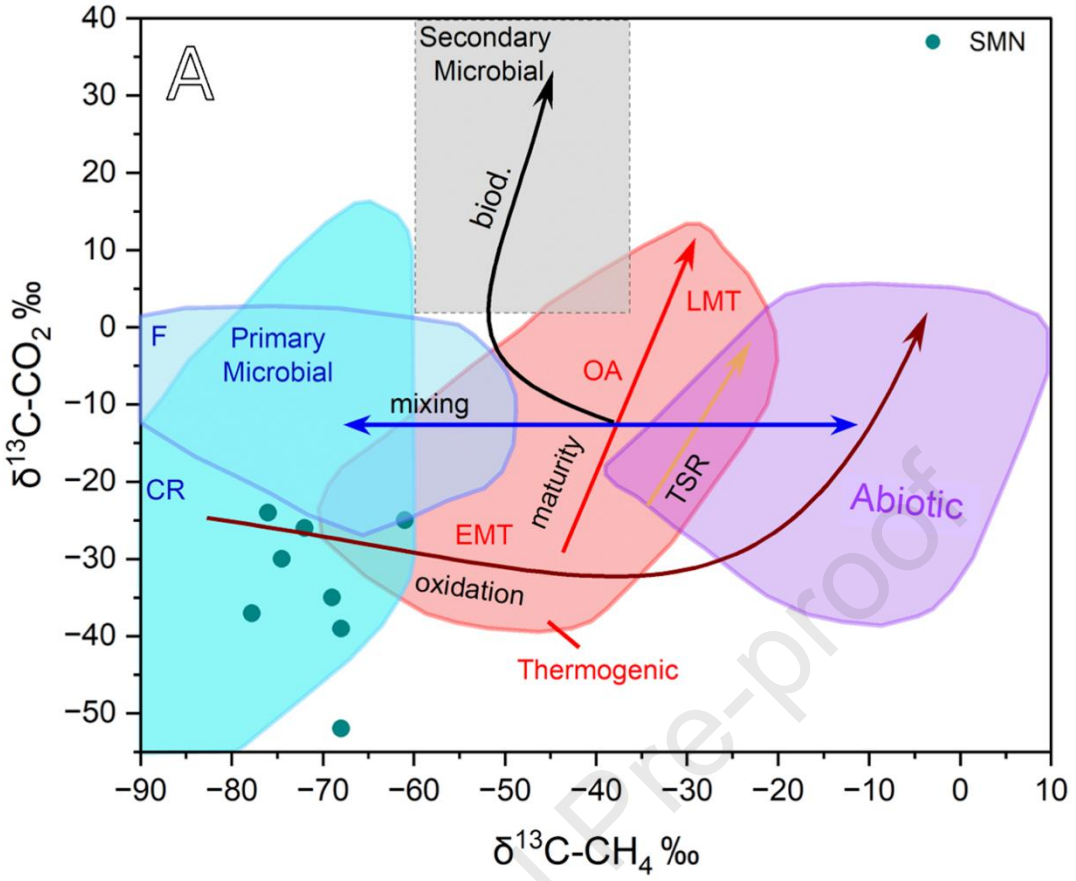

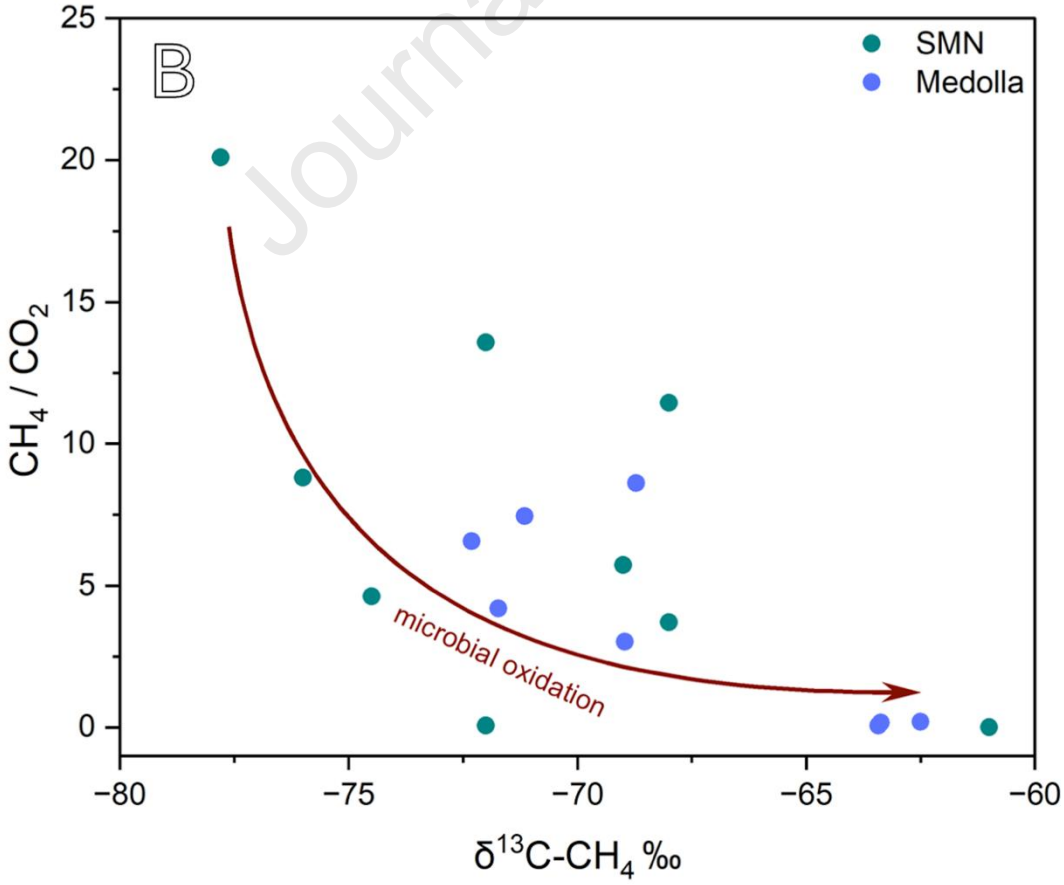

697

Figure 4. (a) SMN soil gas samples are plotted on a diagram of $\delta^{13}C\text{-}CH_4$ versus $\delta^{13}C\text{-}CO_2$, which includes genetic fields and processes influencing the carbon isotopic composition of CH_4 and CO_2 in natural gases, as proposed by Milkov and Etiope (2018). Field acronyms denote CO_2 reduction (CR), methyl-type fermentation (F), secondary microbial (SM), early mature thermogenic gas (EMT), oil-associated thermogenic gas (OA), and late mature thermogenic gas (LMT); while process acronyms represent biodegradation (biod.) and thermochemical sulphate reduction (TSR). (b) Binary diagram of $\delta^{13}C\text{-}CH_4$ versus CH_4/CO_2 ratio for the SMN soil gas samples (green) and the Terre Calde di Medolla soil gas samples (cyan) taken from Capaccioni et al. (2015).

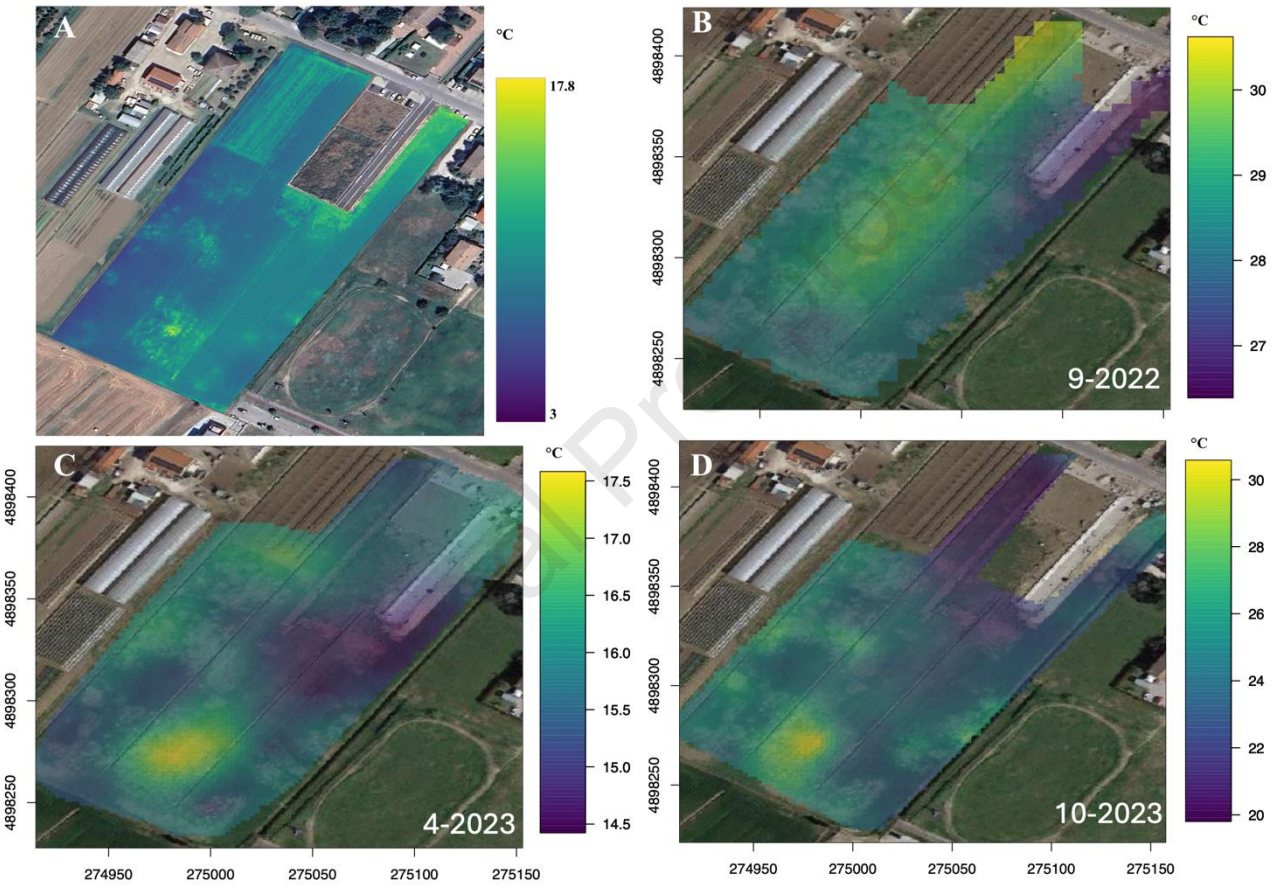

Figure 5. Orthomosaic image captured by the drone with a thermal camera (a) and thermal maps generated using sGs interpolation from ground measurements (b, c, and d).

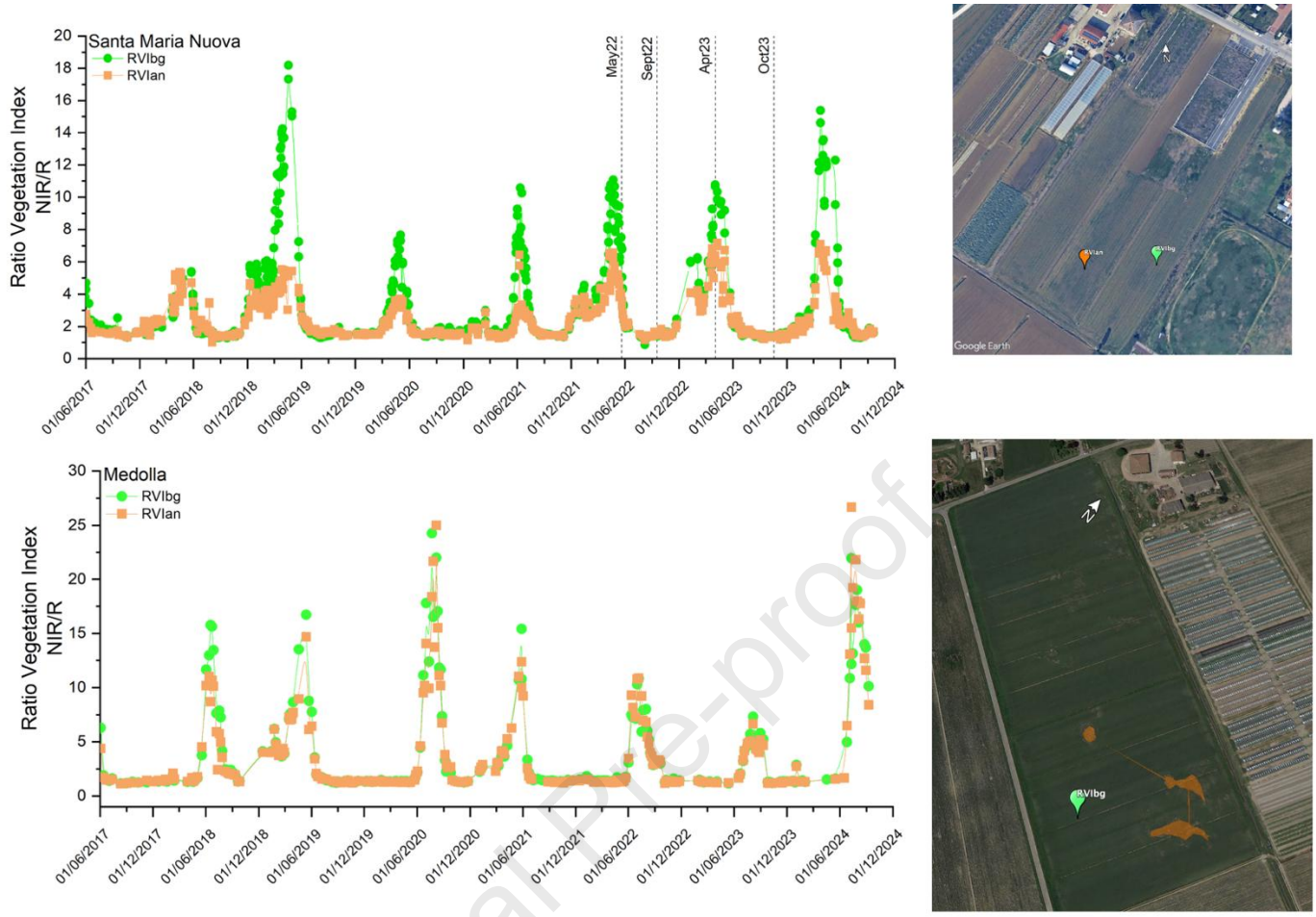

Fig. 6. Time series of the Ratio Vegetation Index (RVI) derived from Sentinel-2 data for the SMN site (upper panel) and Terre Calde di Medolla site (lower panel) over the 2017-2024 period. At each site, RVI was calculated both over vegetated background areas (RVI_{bg}, in green) and over zones affected by CH_4 seepage (RVI_{an}, in orange). The satellite images display the points from which the indices were derived. Dashed vertical lines in the SMN panel mark the dates of the four gas flux surveys conducted in May 2022, September 2022, April 2023, and October 2023.

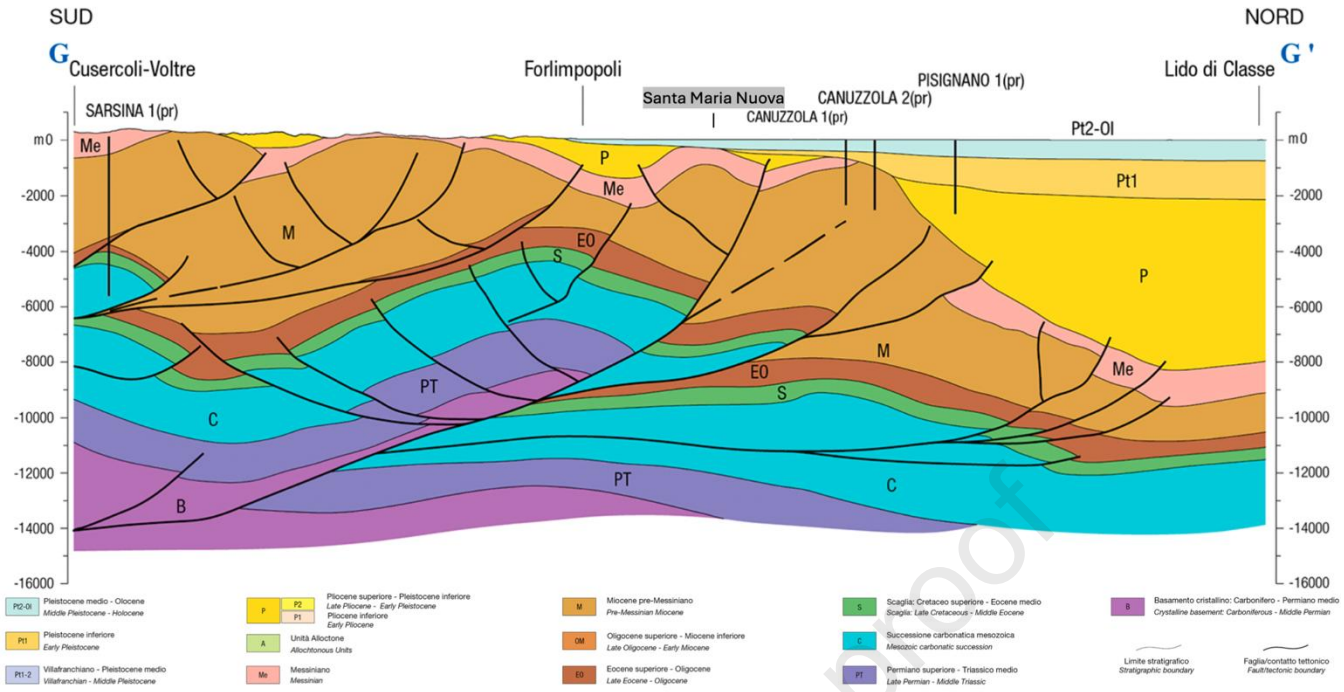

724 Figure 7. The cross-section G-G', the trace of which is taken from the seismotectonic map in Fig. 1b (Emilia-Romagna
725 Region, 2016), illustrates the geological setting of the subsurface of the study area, located between Forlimpopoli and the
726 Cannuzzuola I well.

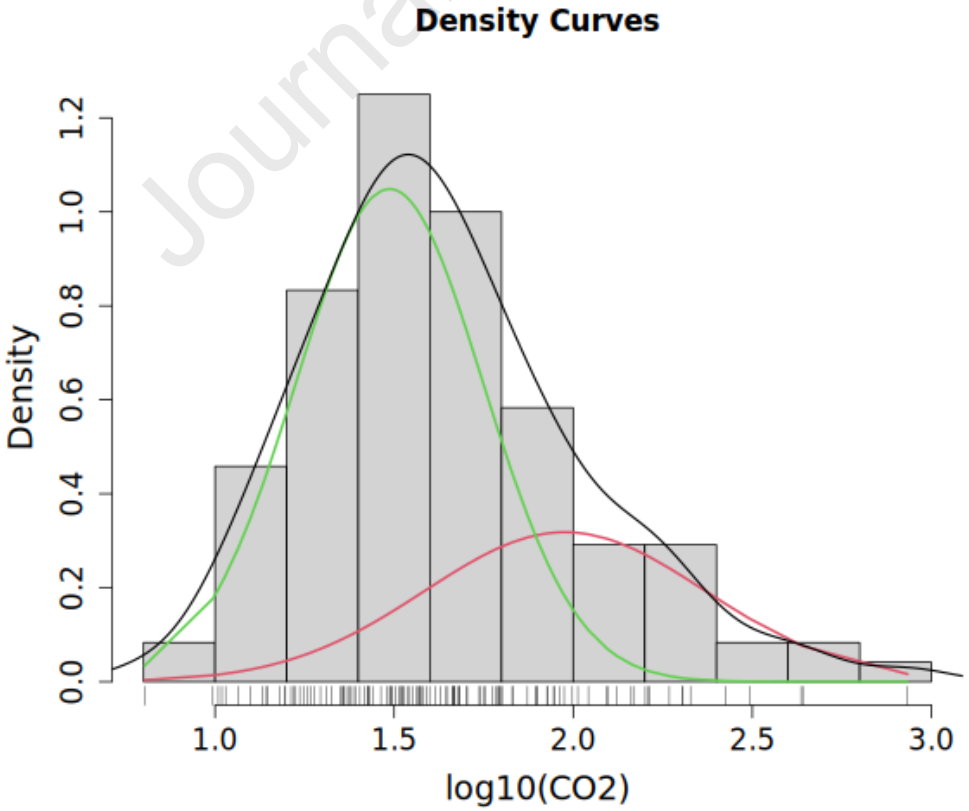

Figure 8. The mixing plot for the September 2022 flux campaign was created using the logarithm of CO_2 fluxes. The plot illustrates the proportion of the two CO_2 mixing factors, along with the mean value (mu) for each population: soil respiration in red and methane oxidation in green.

SUPPLEMENTARY MATERIAL

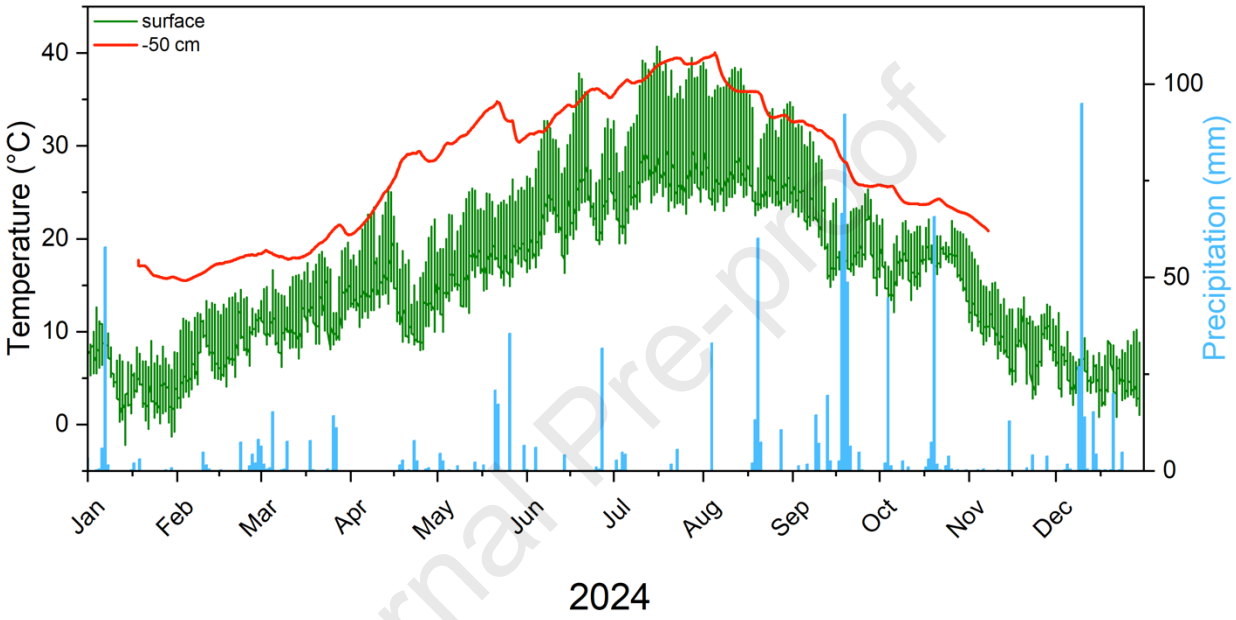

Figure S1. Time series of the SMN anomaly soil temperature (in red) compared with ground temperature (in green, satellite data from ERA5) and daily precipitation (in light blue, data from Weather Underground https://www.wunderground.com/dashboard/pws/IEMILIAR241).

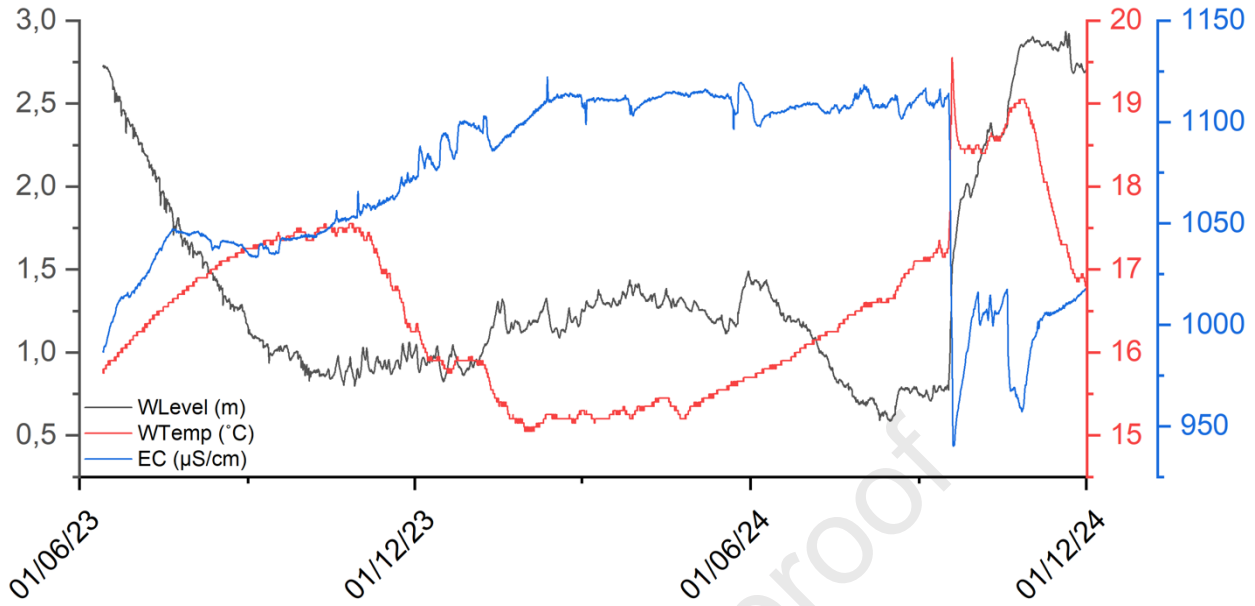

Figure S2. Monitoring time series of the SMN water well. The trends in temperature, level, and electrical conductivity parameters show no anomalies associated with rising fluids. The elevated initial water level of spring 2023 is due to heavy rainfall in May, which affected the entire region. Temperature exhibits a seasonal trend, while electrical conductivity displays fluctuations related to the dynamics of the piezometric level in the well.

ΦCH_4 (g m^{-2} d^{-1})					
	Value Range	**Mean**	**Median**	**Standard Deviation**	**Output in t d^{-1}**
May 2022	0 – 916.9	25.3	11.6	51.3	0.82 ± 0.1
September 2022	0 – 5.8	0.5	0.4	0.4	0.008 ± 0.003
April 2023	0 – 224.4	28.2	18.1	31.7	0.51 ± 0.09
October 2023	0 – 4.6	0.4	0.2	0.5	0.005 ± 0.002

ΦCO_2 (g m^{-2} d^{-1})					
	Value Range	**Mean**	**Median**	**Standard Deviation**	**Output in t d^{-1}**
May 2022	28.2 - 308.5	73.8	63.8	35.8	1.8 ± 0.18
September 2022	9.4 - 174.8	42.4	35.8	24.3	0.62 ± 0.05
April 2023	5.2 - 157.8	37.2	31.7	24.2	0.65 ± 0.07
October 2023	1.9 – 466.1	43.9	26.3	48.3	0.66 ± 0.04

Table 1. Descriptive statistics of the soil diffuse CH_4 and CO_2 flux values for the 2022-2023 surveys (in g m^{-2} d^{-1}) and total output in t d^{-1}.

ID	Date	O_2 vol %	N_2 vol %	CH_4 vol %	CO_2 vol %	CH_4/CO_2	$\delta^{13}C$-CH_4 ‰ V-PDB	$\delta^{13}C$-CO_2 ‰ V-PDB
22A	2022/09/23	19.7	75.5	0.00074	0.09	0.01	-61	-25
22B	2022/09/23	4.7	61.7	29.78	6.43	4.63	-74.5	-30
23A	2023/04/04	19.99	78.71	0.95	0.07	13.57	-72	-26
23A*	2023/04/04	19.99	77.65	1.03	0.09	11.44	-68	-39
23B	2023/04/04	17.73	72.57	7.05	1.23	5.73	-69	-35
23C	2023/04/04	17.74	72.14	7.74	0.88	8.8	-76	-24
23D	2023/04/04	8.25	59.29	25.57	6.88	3.72	-68	-52
23E	2023/04/04	6.07	37.61	54.08	2.69	20.1	-77.8	-37
23F	2023/04/04	20.03	78.32	0.01	0.15	0.07	-72	-

Table 2. Displays the sample ID, date, depth, chemical composition in vol%, and the CH_4/CO_2 ratio, along with the isotopic carbon ratios of CO_2 and CH_4 expressed as $\delta^{13}C$ ‰V-PDB for the interstitial gases at the SMN field. The analysis for sample 23A* relates to a slightly greater depth of 35 cm.

Declaration of interests

☒ The authors declare that they have no known competing financial interests or personal relationships that could have appeared to influence the work reported in this paper.

☐ The authors declare the following financial interests/personal relationships which may be considered as potential competing interests: